

Quantum Otto Heat Engine based on the Dicke-Stark Model under Infinite-Time and Finite-Time Thermodynamic Frameworks

Weilin Wang,¹ Xiyuan Zhang,¹ Weiran Zhao,¹ Mingshu Zhao,¹ Jinying Ma,¹ and Zhanyuan Yan^{1, 2, *}

¹*Department of Mathematics and Physics, North China Electric Power University, Huadian Road, Baoding 071000, China*

²*Hebei Key Laboratory of Physics and Energy Technology,*

North China Electric Power University, Baoding 071003, China

(Dated: August 15, 2025)

We propose a quantum Otto heat engine that employs a finite-size Dicke-Stark model as the working substance. In the extended coherent state space, the complete energy spectrum and eigenstates of this model are obtained through numerical calculations. Within the infinite-time and finite-time thermodynamics frameworks, we investigate the effects of the Stark field strength, coupling strength, adiabatic stroke time, isochoric stroke time, and number of atoms in the DS model on the heat engine's output work, efficiency, and power. The results show that the maximum values of the output work and efficiency appear near the coupling strength corresponding to the superradiant phase transition point. Regulating the Stark field strength can tune the energy level structure of the system and the superradiant phase transition, effectively reducing entropy generation and quantum friction during nonequilibrium evolution of the system's states and thereby significantly increasing the engine's output work, efficiency, and power. Asymmetric heat engines, where the two isochoric strokes have different Stark field strengths and stroke times, are more conducive to optimizing the heat engine's performance. Additionally, in the DS model, an increase in the number of atoms is also beneficial for increasing the heat engine's output work and efficiency. The results of this paper facilitate the design of high-performance quantum heat engines.

I. INTRODUCTION

Quantum heat engines have recently attracted significant attention due to their potential as microscale energy conversion devices and their promising applications in nanotechnology [1, 2]. Unlike conventional heat engines, quantum heat engines employ quantum systems as their working substance, such as cavity quantum electrodynamics (QED) systems that describe the interaction between qubits and quantum light fields [3–6]. Consequently, these engines can leverage the quantum properties of the system, including entanglement and coherence, to achieve performance that reaches or even exceeds traditional thermodynamic limits [7, 8]. Experimentally, quantum heat engines have been realized on various platforms, including trapped-ion systems [9], optomechanical platforms [10, 11], ultracold atomic ensembles [12] and superconducting circuits [13, 14].

The thermodynamic cycle is central to the design of quantum heat engines, with typical cycles including the Carnot cycle, Otto cycle, and Stirling cycle [15–18]. Among these, the quantum Otto cycle is a primary research focus due to its simplicity and ease of quantization. This cycle comprises two isochoric processes and two adiabatic processes: During isochoric processes, the working substance exchanges heat with a heat reservoir, whereas in adiabatic processes, the energy levels of the working substance are adjusted by an external field. Efficiency and output work serve as key metrics for evaluating the performance of a heat engine. Previous studies often assumed quasistatic operation with an infinite cycle time,

which achieves an efficiency close to the Carnot limit but results in zero power output [19–21]. However, practical applications require balancing efficiency and power within a finite time, and this challenge has driven the development of finite-time quantum thermodynamics, highlighting the crucial impact of quantum friction and nonadiabatic transitions [22–24] on engine performance.

Enhancing the performance of a quantum heat engine involves two key strategies:

First, the energy output is maximized through the selection of the working substance. The working substances currently under extensive investigation include, oscillator systems [25], spin systems [26], quantum gases [27, 28], and many-body quantum systems [29]. As a representative of many-body systems, the Dicke model describes the collective coupling of N two-level atoms to a single-mode light field [30]. A crucial characteristic of the Dicke model is the superradiant phase transition (SPT): When the coupling strength exceeds a critical threshold, the ground state of the system undergoes an abrupt transition from a normal phase characterized by a low photon number to a superradiant phase, marked by macroscopic photon occupation and collective atomic polarization [31, 32]. The associated critical fluctuations and many-body entanglements can significantly increase the energy transport efficiency [33, 34].

Second, the energy losses are minimized via nonequilibrium control. Recent developments in finite-time quantum thermodynamics indicate that nonequilibrium dissipation can be effectively prevented by optimizing external field control protocols, such as shortcuts to adiabaticity (STAs) [22, 35–38], and the energy transfer efficiency can be increased through counterdiabatic driving fields that effectively prevent nonequilibrium dissipation [39–42].

* Contact author:yanzhanyuan@ncepu.edu.cn

pation [39, 40]. Additionally, the performance of many-body heat engines is sensitive to the superradiant phase transition. Controlling the superradiant phase transition point with an external field can effectively reduce quantum friction and increase the efficiency of a heat engine [29, 41–45].

Based on the above two strategies, the Dicke–Stark (DS) model has emerged as a promising candidate for working substances. By applying an external electric field, the energy difference of the two-level atom and the superradiant phase transition point in this model can be modified. Rational control of the external electric field, nonequilibrium quantum dissipation and quantum friction can be effectively reduced, thereby improving the performance of the heat engine.

The solution from the DS model also presents a significant challenge. When the atom–field coupling strength reaches ultrastrong or deep–strong coupling regimes, the rotating wave approximation (RWA) is no longer valid [46, 47]. In such cases, only partial results such as ground state and phase transitions can be obtained at the thermodynamic limit (where the number of atoms $N \rightarrow \infty$) by exploiting the collective symmetry of the Dicke system [48, 49]. However, the calculation of the overall energy spectra and eigenstates of the infinite-size DS model remains an unsolved issue. Consequently, the finite-size DS model has become a viable working substance for research, particularly within the coherent-state basis where computational demands are substantially reduced, enabling efficient calculation of the system’s energy spectrum and corresponding wavefunctions. Furthermore, in the strong coupling regimes, only the dressed-state solution from the model can describe the quantum state of the system. Therefore, formulating and solving the dressed master equation constitutes the foundation for studying quantum heat engines within the framework of finite-time thermodynamics [50–52].

In this work, we employ the Dicke–Stark model as the working substance to investigate a four-stroke quantum Otto cycle heat engine. The remainder of this paper is organized as follows: In Section II, the dressed master equation of the quantum DS model and its numerical solution methods on a coherent-state basis are presented. In Section III, the working cycle process of the four-stroke quantum heat engine is introduced. The optimization of heat engine performance under the infinite-time and finite-time thermodynamic frameworks is investigated in detail in Sections IV and V, respectively. The main findings are summarized in Section VI.

II. MODELS AND METHODS

A. Dicke–Stark Model

The Dicke–Stark model describes a quantum system composed of N two-level qubits interacting with a single-mode bosonic field. The Hamiltonian of the system can

be expressed as ($\hbar = 1$ and $k_B = 1$) [53–57] :

$$\hat{H}_{DS} = \omega \hat{a}^\dagger \hat{a} + \Delta \hat{J}_z + \frac{2\lambda}{\sqrt{N}} (\hat{a}^\dagger + \hat{a}) \hat{J}_x + \frac{U}{N} \hat{a}^\dagger \hat{a} \hat{J}_z, \quad (1)$$

where \hat{J}_x and \hat{J}_z represent the collective spin operators, composed of $\hat{J}_\alpha = \sum_{i=1}^N \frac{1}{2} \hat{\sigma}_\alpha^i$, with $\hat{\sigma}_\alpha (\alpha = x, y, z)$ as the Pauli operators. \hat{a}^\dagger and \hat{a} denote the creation and annihilation operators of the bosonic field. Δ and ω represent the frequency of the qubits and the single bosonic mode, and λ is the qubit–boson coupling strength. U represents the intensity of the nonlinear Stark interaction. In the following sections, we set the bosonic frequency ω as the energy unit for simplicity.

Owing to the unavailability of complete eigenenergy and eigenstate information for the DS model in the thermodynamic limit ($N \rightarrow \infty$), we select the finite-size DS model as the working substance for our heat engine. Numerically calculating the eigenenergies and eigenstates of the finite-size DS model in the Fock state space of the bosonic field requires a large photon number cutoff to ensure computational accuracy; this leads to the challenge of solving a Hamiltonian matrix with enormous dimensions, which poses a great challenge to computer memory and computation time.

B. Extended Coherent Bosonic State Approach

The extended coherent bosonic state approach is proposed for accurately calculating the eigenenergies and eigenstates of the finite-size Dicke model using a small photon number cutoff [48]. This method is also applicable to the finite-size DS model [58], making it possible to study heat engines with the DS model as the working substance. Before including the extended coherent bosonic state method, we rotate the collective spin operators with $\pi/2$ along \hat{J}_y by $\hat{H} = \exp(i\pi\hat{J}_y/2)\hat{H}_D\exp(-i\pi\hat{J}_y/2)$, resulting in

$$\hat{H} = \omega \hat{a}^\dagger \hat{a} - \left(\frac{\Delta}{2} + \frac{U}{2N} \hat{a}^\dagger \hat{a}\right) (\hat{J}_+ + \hat{J}_-) + \frac{2\lambda}{\sqrt{N}} (\hat{a}^\dagger + \hat{a}) \hat{J}_z. \quad (2)$$

in which $\hat{J}_\pm = \hat{J}_x \pm i\hat{J}_y$ are the raising and lowering operators of the atomic states $\{|j, m\rangle, m = -j, -j+1, \dots, j-1, j\}$ with $j = N/2$. Then, the states in the Hilbert space of the entire system can be represented by the direct product of the bosonic field states and the atomic states, $\{|\varphi^n\rangle_b \otimes |j, m\rangle\}$.

Considering a displacement operator $\hat{D}(g_m) = \exp(g_m \hat{a} - g_m \hat{a}^\dagger)$, with $g_m = 2\lambda m / \omega \sqrt{N}$, the displaced operators $\hat{A}_m = \hat{D}^\dagger \hat{a} \hat{D} = \hat{a} + g_m$, $\hat{A}_m^\dagger = \hat{D}^\dagger \hat{a}^\dagger \hat{D} = \hat{a}^\dagger + g_m$ serve as the creation and annihilation operators of the extended coherent state space, which is defined as follows:

$$|k\rangle_{A_m} = \frac{1}{\sqrt{k!}} (\hat{A}_m^\dagger)^k |0\rangle_{A_m},$$

where $|0\rangle_{A_m} = \hat{D}^\dagger |0\rangle_a$ is the vacuum state in the extended coherent state space.

Then, the photonic state can be expanded in the extended coherent state space as

$$|\varphi_m^n\rangle_b = \sum_{k=0}^{N_{tr}} \frac{1}{\sqrt{k!}} C_{m,k}^n (\hat{A}_m^\dagger)^k |0\rangle_{A_m}$$

Obviously, the expansion of the photonic state in the extended coherent state space includes all Fock states; thus, a relatively small truncation number N_{tr} can yield accurate calculation results. Substituting the state of the entire system into the Schrodinger equation yields the following:

$$\begin{aligned} & \sum_{m,k} \omega C_{m,k}^n (k - g_m^2) |j, m\rangle |k\rangle_{A_m} \\ & - \sum_{m,k} C_{m,k}^n \left[\frac{\Delta}{2} + \frac{U}{2N} (k + g_m^2) \right] (j_m^+ |j, m+1\rangle |k\rangle_{A_m} + j_m^- |j, m-1\rangle |k\rangle_{A_m}) \\ & + \frac{U}{2N} \sum_{m,k} C_{m,k}^n g_m (\sqrt{k+1} j_m^+ |j, m+1\rangle |k+1\rangle_{A_m} + \sqrt{k} j_m^+ |j, m+1\rangle |k-1\rangle_{A_m}) \\ & + \frac{U}{2N} \sum_{m,k} C_{m,k}^n g_m (\sqrt{k+1} j_m^- |j, m-1\rangle |k+1\rangle_{A_m} + \sqrt{k} j_m^- |j, m-1\rangle |k-1\rangle_{A_m}) \\ & = E_n \sum_{m,k} C_{m,k}^n |j, m\rangle |k\rangle_{A_m}. \end{aligned} \quad (3)$$

We then multiply $\{\langle l | \langle n, j |\}$ by $n = -j, -j+1, \dots, j$. We obtain the equation satisfied by the expansion coefficients $C_{m,k}^n$

$$\begin{aligned} & \omega C_{n,l}^n (k - g_n^2) \\ & - \left[\frac{\Delta}{2} + \frac{U}{2N} (k + g_{n-1}^2) \right] C_{n-1,l}^n j_{n-1}^+ \sum_k \langle l | k \rangle_{A_{n-1}} \\ & + \left[\frac{\Delta}{2} + \frac{U}{2N} (k + g_{n+1}^2) \right] C_{n+1,l}^n j_{n+1}^- \sum_k \langle l | k \rangle_{A_{n+1}} \\ & + \frac{U}{2N} C_{n-1,k}^n g_{n-1} \sqrt{k+1} j_{n-1}^+ \sum_k \langle l | k+1 \rangle_{A_{n-1}} \\ & + \frac{U}{2N} C_{n-1,k}^n g_{n-1} \sqrt{k} j_{n-1}^+ \sum_k \langle l | k-1 \rangle_{A_{n-1}} \\ & + \frac{U}{2N} C_{n+1,k}^n g_{n+1} \sqrt{k+1} j_{n+1}^- \sum_k \langle l | k+1 \rangle_{A_{n+1}} \\ & + \frac{U}{2N} C_{n+1,k}^n g_{n+1} \sqrt{k} j_{n+1}^- \sum_k \langle l | k-1 \rangle_{A_{n+1}} \\ & = E_n C_{n,l}^n, \end{aligned} \quad (4)$$

in which the inner products are

$$\langle A_n | l | k \rangle_{A_{n-1}} = (-1)^l D_{l,k,A_n} \langle l | k \rangle_{A_{n+1}} = (-1)^k D_{l,k},$$

$$D_{l,k} = e^{-G^2/2} \sum_{r=0}^{\min(l,k)} \frac{(-1)^{-r} \sqrt{l!k!} G^{l+k-2r}}{(l-r)!(k-r)!r!}, \quad G = \frac{2\lambda}{\omega\sqrt{N}}.$$

Notably, the theoretical range for the Stark field strength parameter U is $[-\infty, 2\omega]$ [58]. However, considering experimental feasibility and the need for many photons to obtain accurate energy levels as U increases, in the subsequent research, we limited the range of U to $|U| < \omega$ and adopted a maximum truncation number $N_{tr} = 60$. This parameter setting is sufficient to ensure that the calculated excitation state energies converge to the target accuracy within the $|U| < \omega$ region, with a relative error less than 10^{-4} .

C. Quantum Dressed Master Equation

According to the method outlined in [59–61], we can derive the thermodynamically effective master equation for the entire Hamiltonian spectrum, which holds under weak damping conditions: A high reservoir cutoff frequency and a flat spectral density ensure that the system is positive and has Markovian properties. Under these conditions, the system dynamics are governed by the dressed-state master equation [50–52, 62–65]

$$\begin{aligned} \frac{d}{dt} \hat{\rho} = & -i[\hat{H}, \hat{\rho}] + \sum_{\substack{u=a,\sigma^- \\ k < j}} \{ \Gamma_u^{jk} n_u(\Delta_{jk}) D[|\phi_j\rangle\langle\phi_k|, \hat{\rho}] \\ & + \Gamma_u^{jk} [1 + n_u(\Delta_{jk})] D[|\phi_k\rangle\langle\phi_j|, \hat{\rho}] \}, \end{aligned} \quad (5)$$

where $D[\hat{O}, \hat{\rho}] = \hat{O}\hat{O}^\dagger - \frac{1}{2}\{\hat{O}^\dagger\hat{O}, \hat{\rho}\}$. The dissipation rates $\Gamma_u^{jk} = \gamma_u(\Delta_{jk})|S_u^{jk}|^2$ depend on the spectral function $\gamma_u(\Delta_{jk})$ and the transition coefficients $S_u^{jk} = \langle\phi_j|(\hat{a}^\dagger + \hat{a})|\phi_k\rangle$ and $S_{\sigma^-}^{jk} = \langle\phi_j|(\hat{\sigma}_+ + \hat{\sigma}_-)|\phi_k\rangle$. For the ohmic case, $\gamma_u(\Delta_{jk}) = \pi\alpha\Delta_{jk} \exp(-|\Delta_{jk}|/\omega_c)$, where α represents the coupling strength and where ω_c represents the cutoff frequency; throughout all the numerical simulations performed, we consider $\alpha = 0.001\omega$ and $\omega_c = 10\omega$. The Bose–Einstein distribution $n_u(\Delta_{jk}, T_u) = 1/[\exp(\Delta_{jk}/T_u) - 1]$ accounts for thermal effects. The steady-state solution to Eq. (5) yields the density matrix of the canonical ensemble, as confirmed by straightforward numerical simulations:

$$\hat{\rho}_{ss} = \sum_n \frac{e^{-E_n/T}}{Z} |\phi_n\rangle\langle\phi_n|. \quad (6)$$

where $Z = \sum_n e^{-E_n/T}$ represents the partition function and $P_n^{ss} = \frac{e^{-E_n/T}}{Z}$ is the population.

III. QUANTUM OTTO CYCLE

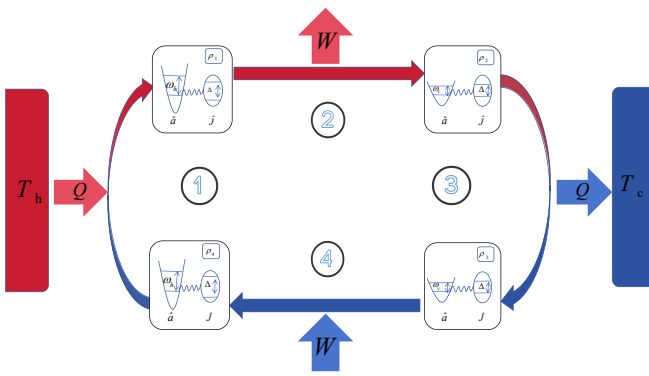


FIG. 1. Schematic diagram of a four-stroke Otto cycle quantum heat engine based on the Dicke–Stark model. Processes 1 (3) represent isochoric heating (cooling), where the working substance interacts with a hot (cold) reservoir at temperature $T_h (T_c)$. The frequency remains constant, heat is absorbed (released), and no work is performed. Process 2 (4) represents adiabatic expansion (compression), where the working substance is isolated from heat reservoirs. The frequency is changed from $\omega_h (\omega_c)$ to $\omega_c (\omega_h)$. The system energy shifts from $E_h (E_c)$ to $E_c (E_h)$. No heat is exchanged, and the system performs positive (negative) work on the outside.

The quantum Otto engine works by cyclically manipulating the parameters of the working substance, including four main stages: isochoric heating, adiabatic expansion, isochoric cooling and adiabatic compression [22]. The thermodynamic cycle that we consider is shown in Fig. 1.

Quantum isochoric heating process: A working substance characterized by Hamiltonian H^h and frequency ω_h contacts a hot reservoir at temperature (T_h) and gradually heats. The state of the system evolves from $\rho(T_c)$ to $\rho(T_h)$ without performing any work, and the heat absorbed during this process is Q_h .

Quantum adiabatic expansion process:

The system is isolated from heat reservoirs. By changing its frequency from ω_h to ω_c ($\omega_h > \omega_c$), the energy levels change from E_n^h to E_n^c . During this process, output work W is performed without heat exchange.

Quantum isochoric cooling process: The working substance, with a frequency of ω_c , contacts a cold reservoir at temperature $T_c < T_h$. The state of the system evolves from $\rho(T_h)$ to $\rho(T_c)$ without performing any work, and the heat absorbed during this process is Q_c .

Quantum adiabatic compression process: Isolated from the cold reservoir, the energy levels of the system change from E_n^c to E_n^h as the frequency changes from ω_c to ω_h . Input work W is performed without heat exchange.

A positive value of Q indicates that the working substance absorbs heat from the reservoir, whereas a negative value indicates heat release. Similarly, positive values of W indicate the output work of the engine, and

negative values indicate input work on the heat engine. The allowed working regimes under the Clausius inequality and the first law of thermodynamics are as follows:

Heat engine (E): $Q_h > 0, Q_c < 0, W > 0$;

Refrigerator (R): $Q_c > 0, Q_h < 0, W > 0$;

Heater (H): $Q_c < 0, Q_h < 0, W < 0$;

Accelerator (A): $Q_c < 0, Q_h > 0, W < 0$.

Among these four operation modes, the heat engine (E) and the refrigerator (R) are of the most practical. In this work, we focus on the heat engine, which operates by absorbing heat from a hot reservoir, converting part of this energy to work, and releasing the remaining heat to a cold reservoir.

IV. INFINITE-TIME CYCLE

A. Work and Heat Calculations

The first law of thermodynamics for quantum systems with discrete energy levels is expressed as follows[66]:

$$dU = \delta Q + \delta W = \sum_n (E_n dP_n^{ss} + P_n^{ss} dE_n). \quad (7)$$

where E_n represents the energy levels and where P_n^{ss} represents the probabilities of steady-state occupation. The heat Q_h and Q_c exchange with the hot reservoir and the cold reservoir, respectively, and the net work W is expressed as follows:

$$Q_h = \sum_n E_n^h [P_n^{ss}(T_h) - P_n^{ss}(T_c)], \quad (8)$$

$$Q_c = \sum_n E_n^c [P_n^{ss}(T_c) - P_n^{ss}(T_h)], \quad (9)$$

$$W = Q_h + Q_c = \sum_n (E_n^h - E_n^c) [P_n^{ss}(T_h) - P_n^{ss}(T_c)]. \quad (10)$$

The efficiency of the heat engine, η , is a key figure of merit and is defined as the ratio of the work output to the heat absorbed from the hot reservoir.

$$\eta = \frac{W}{Q_h}. \quad (11)$$

B. Operational Modes in the Infinite-time Cycle

We begin by investigating the effects of the reservoir temperature T , the coupling strength λ , and the Stark field strength U on the operational modes of the quantum thermal machine. The phase diagram depicting the operating states of the quantum Otto heat machine is shown in Fig. 2. The results show that significant changes occur in the phase diagram of the operational modes

when the temperature of the hot reservoir (or cold reservoir) is fixed while the temperature of the cold reservoir (or hot reservoir) is varied. For large temperature differences, the phase diagram is dominated by the heat engine mode [pink regions, Figs. 2(e)- 2(h)]; conversely, for small temperature differences, the refrigeration mode (blue regions) dominates, as shown in Figs. 2(a)- 2(d). Under appropriate coupling strength, tuning the Stark field strength of U enables the heat engine to switch from one operating mode to another. Notably, as shown in the enlarged image in Fig. 2(b), when the coupling strength is approximately 0.1ω , precise tuning of U facilitates transitions among four distinct operational modes. These characteristics have substantial potential for developing tunable, multifunctional quantum thermal devices.

C. Optimization of Output Work and Efficiency in the Infinite-time Cycle

Under quasistatic conditions, the study of the work output and efficiency of a heat engine is crucial for designing heat engines with excellent performance. We use Eq. 10 and Eq. (11) to calculate the work output and efficiency under quasistatic conditions. Strategically tuning both the coupling strength λ and the Stark field strength U enables the heat engine to achieve optimal work output and efficiency, corresponding to the red shaded regions in Figs. 3(a) and (b), respectively.

To elucidate the regulatory effect of U on the output work and efficiency of the heat engine, discrete analyses of U are shown in Fig. 4. First, when U is held constant, both the output work W and the efficiency η increase gradually with increasing coupling strength λ , reach a peak and then decrease rapidly.

Next, by comparing the curves of the heat engine's output work and efficiency as functions of the coupling strength for different values of U , the results presented in Fig. 4(a) and Fig. 4(b) demonstrate that as U increases, the peak of the output work gradually increases, whereas the corresponding coupling strength λ gradually decreases. This behavior is advantageous for the fabrication of heat engines with high output work. In particular, when U is positive, the output work of the heat engine can be optimized. The efficiency curves in Figs. 4(c) and 4(d) indicate that positive U values increase efficiency in the low coupling strength region but reduce peak efficiency. While a negative U increases peak efficiency, the required coupling λ becomes stronger. The results in Fig. 4 provide crucial guidance for the design of heat engines, enabling performance optimization through rational regulation of U and λ .

To clarify the control mechanism of the parameter U , based on the relationship among the coupling strength, efficiency, and work shown in Fig. 4, we identified the extrema and zero points. By using the superradiant phase

transition formula

$$\lambda_c(T) = \sqrt{\frac{\Delta}{4} \left[\frac{\omega}{\tanh(\frac{\Delta}{2k_B T})} - \frac{U}{2} \right]}. \quad (12)$$

We can accurately determine the superradiant phase transition points of the DS model, which are marked in Table I. The chart shows that the coupling strengths corresponding to the zero points and extrema appear near the superradiant phase transition points, and as $|U|$ increases, the degree of agreement between the zero points and phase transition points further increases.

To further improve the performance of heat engines, we investigated an asymmetric quantum heat engine that applies distinct control parameters U during isochoric expansion (second stroke) and isochoric compression (fourth stroke) [67]. In Fig. 5, the optimal work output and efficiency do not occur in symmetric U configurations (i.e., along the diagonal $U_2 = U_4$ in Fig. 5), highlighting the potential of asymmetric modulation U to increase the power and work output. This asymmetric optimization originates from the differential sensitivity of the population distributions to U across temperature regimes. As shown in Fig. 5 (a), the output of work peaks when a positive U is applied in the second stroke and a negative U is applied in the fourth stroke. The efficiency reaches its peak when a negative U is applied in the second and fourth strokes, as illustrated in Fig. 5(b). The divergent control requirements for maximizing work output versus efficiency demonstrate the impossibility of simultaneously optimizing both performance metrics [68].

In the finite-size DS model, the effect of the number of atoms (N) on the performance of the quantum heat engine must be investigated. To explore the limited performance of the heat engine, we focus on the peak values of work output and efficiency. Figure. 6(a) reveals that the maximum output work occurs in a system with $N = 2, 8, 16, 32, 48$ and $U = 0.9$. The system with $N = 48$ achieves the maximum output work. As N increases, the peak of the output work increases slightly, and the values of the maximum output work for $N = 16, 32, 48$ are almost identical. Figure. 6(b) reveals the maximum efficiency at $U = -0.9$ and the same N value as that in Fig. 6(a). The maximum efficiency increases with increasing N , and at $N > 32$, the maximum efficiency is almost no longer affected by the number of atoms N . Although both the maximum efficiency and maximum output work increase with the number of atoms in this figure, this occurs at a specific U . Different values of U may lead to the maximum values being reached at different numbers of atoms. Therefore, in the above discussion, selecting $N = 8$ can balance the optimization of the power output and efficiency of the heat engine.

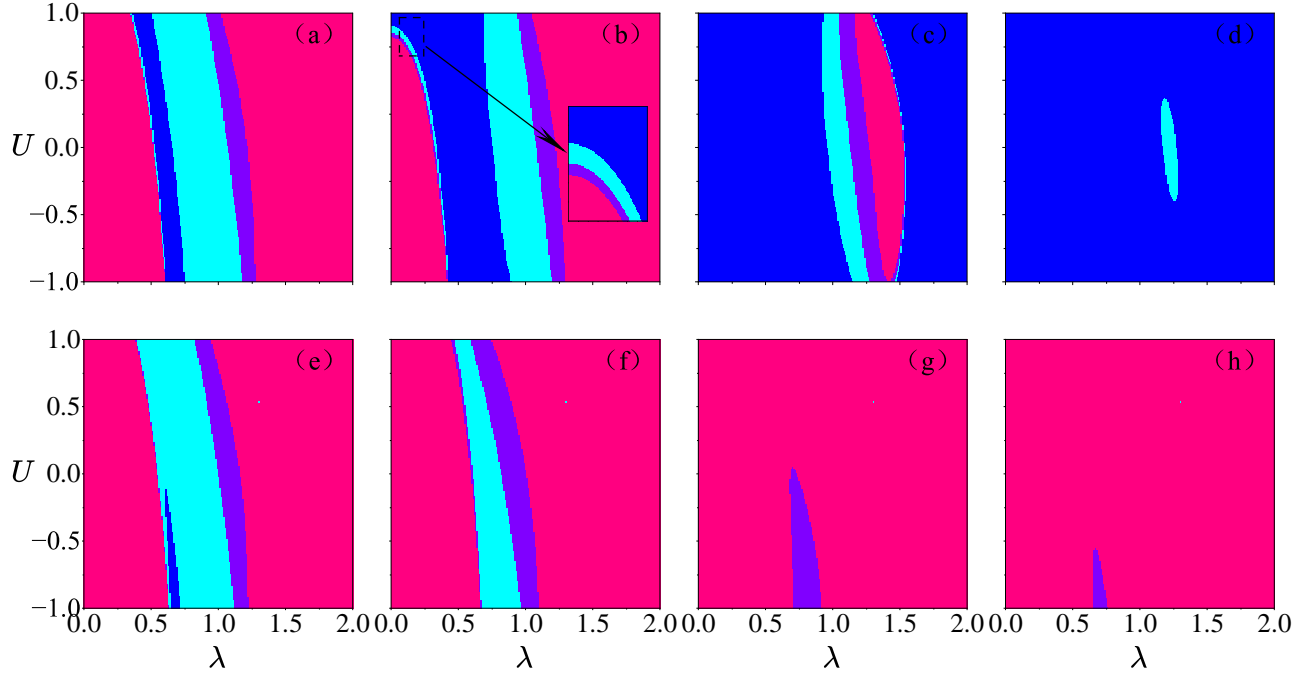


FIG. 2. Operational state diagram of the heat engine defined by two control parameters: coupling strength (horizontal axis) and Stark field strength (vertical axis). Four distinct operational regions are identified: the heat engine region (pink), the refrigerator region (blue), the accelerator region (light blue), and the eater region (purple). The temperatures are (a) $T_c = 0.1$, $T_h = 0.5$, (b) $T_c = 0.2$, $T_h = 0.5$, (c) $T_c = 0.3$, $T_h = 0.5$, (d) $T_c = 0.4$, $T_h = 0.5$, (e) $T_c = 0.1$, $T_h = 0.6$, (f) $T_c = 0.1$, $T_h = 0.8$, (g) $T_c = 0.1$, $T_h = 1.0$, (h) $T_c = 0.1$, $T_h = 1.4$, and $N = 8$, $\omega_h = 2\omega$, $\omega_c = \omega$, $\omega = 1$.

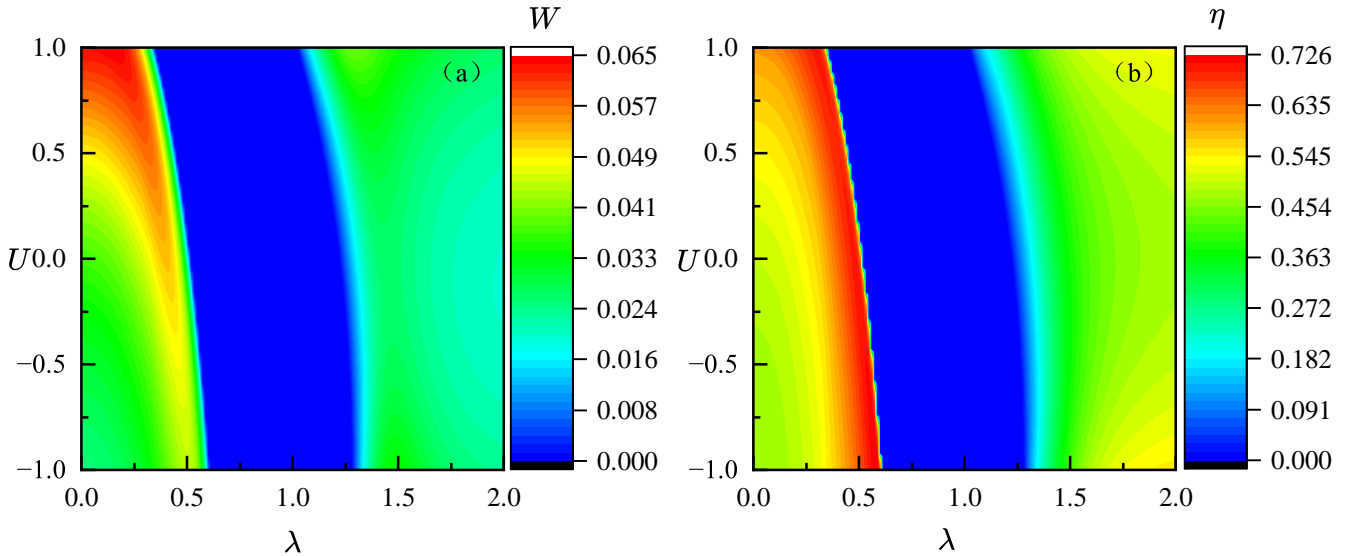


FIG. 3. Analysis of the two-dimensional heat maps of work output (a) and efficiency (b) for the working substance in the quantum Otto cycle based on the DS model. The diagram quantifies the effects of the Stark field strength (U) and coupling strength (λ) on thermodynamic performance, with color bars indicating the magnitudes of W and η . The additional system parameters are $N = 8$, $\omega_h = 2\omega$, $\omega_c = \omega$, $\omega = 1$, $T_c = 0.1$, and $T_h = 0.5$.

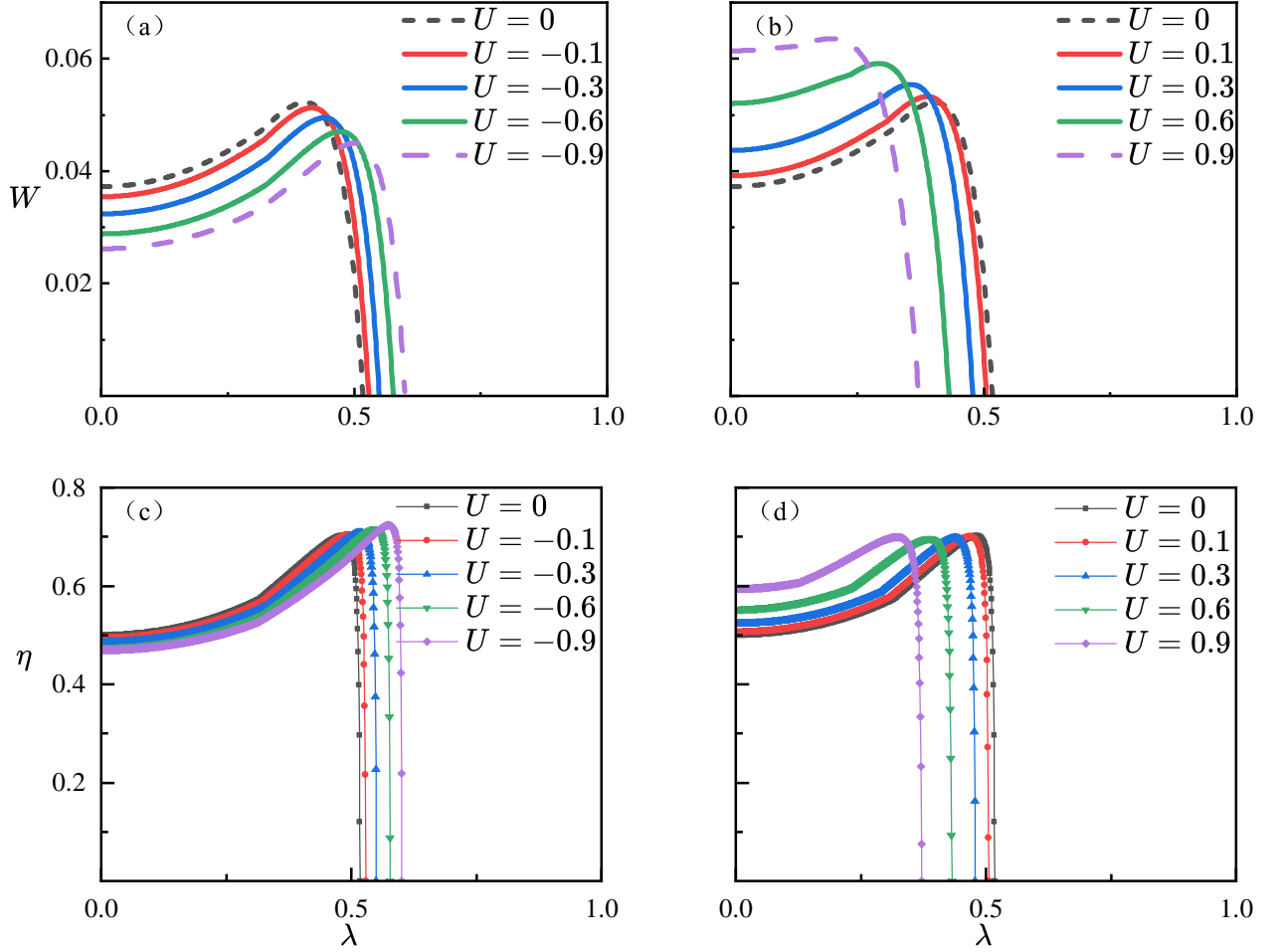


FIG. 4. Work output (a), (b) and efficiency (c), (d) of a thermal engine as a function of the coupling strength λ . The horizontal axis denotes λ , whereas the vertical axis represents the work output (W) and efficiency (η). The curves of different colors represent different Stark field strength U values. The loop parameters include $N = 8$, $\omega_h = 2\omega$, $\omega_c = \omega$, $\omega = 1$, $T_c = 0.1$, and $T_h = 0.5$. All the quantities are measured in units of ω .

TABLE I. Relationship among the hyperradiative phase transition point, efficiency, and work done. The superradiative phase transition is given by formula (1), with $T = 0.1$ and $\omega_c = \omega$.

Stark intensity	$U = -0.9$	$U = -0.6$	$U = -0.3$	$U = -0.1$	$U = 0$	$U = 0.1$	$U = 0.3$	$U = 0.6$	$U = 0.9$
SPT (λ)	0.602	0.570	0.536	0.512	0.500	0.487	0.461	0.418	0.370
efficiency peak(λ)	0.574	0.548	0.517	0.494	0.481	0.468	0.440	0.387	0.323
efficiency zero(λ)	0.601	0.577	0.550	0.529	0.518	0.507	0.479	0.432	0.372
work peak(λ)	0.502	0.470	0.439	0.416	0.401	0.386	0.350	0.29	0.200
work zero(λ)	0.600	0.577	0.549	0.528	0.517	0.504	0.478	0.43	0.370

V. FINITE-TIME CYCLE

A. Work and Heat Calculations

The optimization of quantum heat engines in finite-time operation has attracted significant attention in re-

cent studies, particularly with respect to both increased efficiency and increased power output [69–72]. Theoretically, for the same work output, reducing the cycle duration leads to higher power. However, rapid isochoric expansion and compression strokes cause entropy generation and quantum friction, making the optimization of

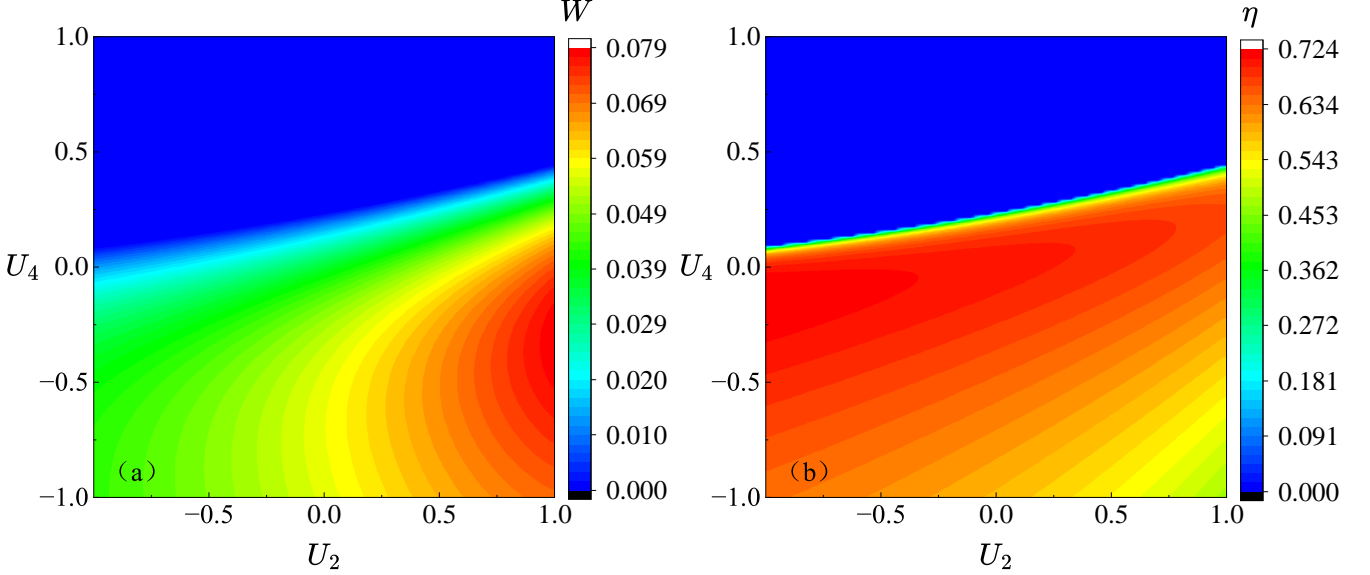


FIG. 5. Based on the two-dimensional heatmap analysis of work output (a) and efficiency (b) for the DS model quantum Otto cycle, the horizontal axis is set to the second stroke Stark field strength U_2 , and the vertical axis is set to the fourth stroke Stark field strength U_4 , with the right-side color bar quantifying the work output and efficiency values. The heatmap reveals that within the control range of the Stark interaction field strength $U_{2(4)} \in [-1, 1]$, the heat engine's performance evolves with the Stark field strength of both strokes. A significant feature is the enhancement effect on work output due to the asymmetric configuration of U_2 and U_4 . The additional system parameters are $\lambda = 0.48$, $N = 8$, $\omega_h = 2\omega$, $\omega_c = \omega$, $\omega = 1$, $T_c = 0.1$, and $T_h = 0.5$.

stroke duration a challenging issue.

To simulate a finite-time Otto cycle, we rigorously derived expressions for work and heat exchange under finite-time constraints from fundamental thermodynamic principles[28].

$$W(t) = \int_0^t dt' \text{Tr} \left\{ \dot{H}(t') \rho(t') \right\}, \quad (13)$$

$$Q(t) = \int_0^t dt' \text{Tr} \left\{ H(t') \dot{\rho}(t') \right\}. \quad (14)$$

Corresponding to the four strokes of the heat engine in Fig. 1, the duration of each stroke is denoted τ_n , where $n = 1, 2, 3, 4$. The two isochoric processes have the same evolution time $\tau_1 = \tau_3$, during which the system exchanges heat with the heat reservoirs without performing any work. During the isochoric heating process, the system absorbs heat from the high-temperature reservoir, evolving from $\rho(T_c)$ to $\rho(T_h)$ within τ_1 . Conversely, during the isochoric cooling process, the system releases heat to the low-temperature reservoir, evolving from $\rho(T_h)$ to $\rho(T_c)$ within τ_3 . The two adiabatic processes have the same evolution time $\tau_2 = \tau_4$, with no heat exchange occurring and only work being done. In the adiabatic expansion process, the frequency of the system evolves linearly from ω_h to ω_c within τ_2 ; the reverse occurs in the adiabatic compression process.

Usually, the evolution of the system's state is regarded as a quasistatic process, where the system is in a thermal equilibrium state described by Eq. (5) at any moment. However, within a finite-time framework, the quasistatic approximation is no longer applicable, and the time evolution of the system's state is governed by the master equation described by Eq. (6). The total entropy generated during a complete cycle of a heat engine is often used to evaluate the impact of finite-time operations on the efficiency of the heat engine. For an Otto cycle heat engine, the total entropy can be expressed as[73–75]

$$\langle \sum_{tot} \rangle = -\frac{1}{T_h} [\text{Tr}(\rho_{t_1} H_h) - \text{Tr}(\rho_{t_4} H_h)] - \frac{1}{T_c} [\text{Tr}(\rho_{t_3} H_c) - \text{Tr}(\rho_{t_2} H_c)]. \quad (15)$$

The efficiency of the quantum engine can be related to the total entropy produced in a cycle as [15, 28, 76],

$$\eta_{th} = \eta_c - \frac{T_c \langle \sum_{tot} \rangle}{\text{Tr}(\rho_{t_1} H_h) - \text{Tr}(\rho_{t_4} H_h)}, \quad (16)$$

where $\eta_c = 1 - \frac{T_c}{T_h}$ represents the efficiency of the Carnot cycle.

B. Quantum Friction

In a finite-time quantum Otto cycle, nonadiabatic transitions during compression and expansion strokes

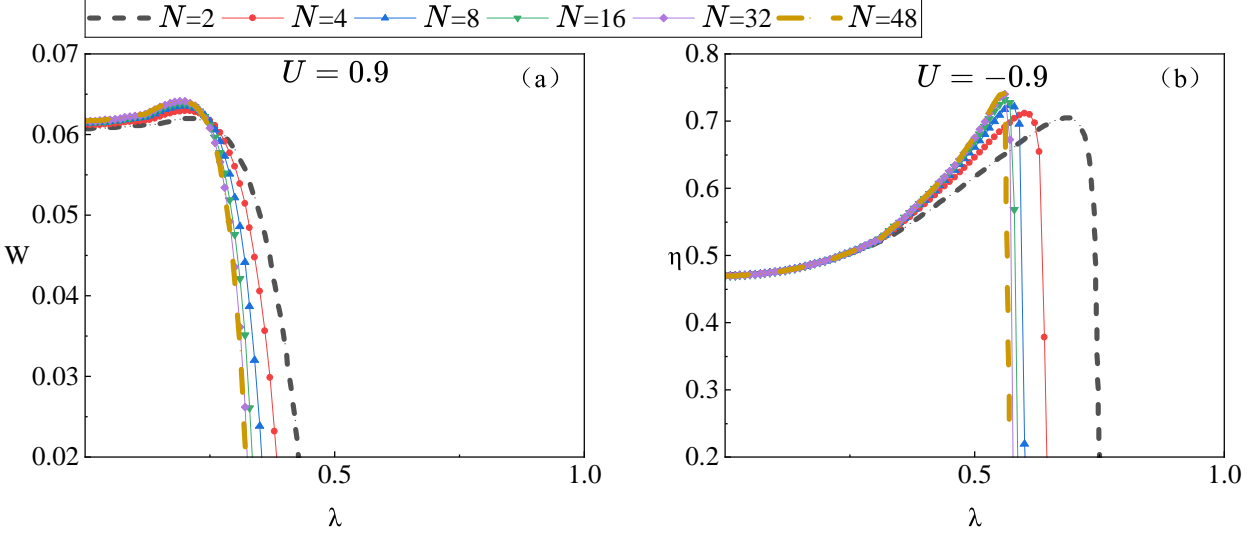


FIG. 6. Figures(a) and (b) Evolution of the work output (W) and efficiency (η) of the quantum heat engine with coupling strength (λ) for different numbers of atoms (N). The horizontal axis represents the coupling strength (λ), and the vertical axis represents the work output (W) and efficiency (η). The multicolored curves correspond to experimental data for different atom numbers, revealing the differences in system performance under finite-size effects. In Fig. (a), $U=0.9$, in Fig. (b), $U=-0.9$, and the additional system parameters are $\omega_h = 2\omega$, $\omega_c = \omega$, $\omega = 1$, $T_c = 0.1$, and $T_h = 0.5$.

generate quantum friction, which converts useful work to dissipated heat[15, 22]. The friction work W_{fric} is defined as follows:

$$W_{\text{fric}} = W_{\text{limited}} - W_{\text{actual}}, \quad (17)$$

where W_{actual} is the actual work output and where W_{limited} can be calculated via Eq. (13). According to the entropy-based framework [29], W_{fric} can be quantified by the quantum relative entropy between the actual state ρ and the adiabatic reference state ρ^{ref} :

$$W_{\text{fric}} = T_{h(c)} D \left(\rho_{2(4)} \parallel \rho_{2(4)}^{\text{ref}} \right), \quad (18)$$

where $D(\rho \parallel \rho^{\text{ref}}) = \text{Tr} [\rho(\ln \rho - \ln \rho^{\text{ref}})]$ and where $\rho_{2(4)}^{\text{ref}}$ represents the instantaneous equilibrium state in the compression (expansion) process. Relative entropy D measures information loss due to finite-time driving. Nonadiabatic transitions between instantaneous eigenstates cause an increase in D , directly reflecting friction-induced work dissipation.

C. Fidelity in Finite-time Cycles

Under finite-time constraints, thermodynamic cycles typically operate in a nonequilibrium state, causing the heat engine's trajectory to deviate from the equilibrium state, which has detrimental effects on the operational stability of the heat engine. Therefore, the evolution of the system state during the multiple cycles of a heat engine must be studied. The system starts the first stroke with a hot Gibbs state ρ_{τ_0} as the initial state, and after

a cycle is completed, it enters the final state ρ_{τ_4} of the fourth stroke. This final state then serves as the starting point ρ_{τ_0} for subsequent cycles, and the operation process continues. After multiple iterations of the cycle are performed, the fidelity of the system state can be defined as

$$F_h = \text{Tr} \sqrt{\sqrt{\rho^{(m-1)}(\tau_0)} \rho^{(m)}(\tau_0) \sqrt{\rho^{(m-1)}(\tau_0)}}, \quad (19)$$

which measures the stability of the heat engine. We calculated the fidelity of the system state within 4 cycles of the heat engine by assuming that the duration of the first or third stroke is finite. As shown in Fig. 7, as the number of cycles increases, the fidelity quickly approaches 1. After four cycles, when $\tau_{1(3)} > 200$, the heat engine tends to stabilize. Therefore, all subsequent simulations were based on five complete cycles, which are sufficient to ensure stable operation of the heat engine.

D. Output Work, Efficiency and Power in the Finite-time Cycle

In this study, we fixed the number of atoms $N = 2$ (since the computational workload under the finite-time framework is extremely heavy, making it difficult to meet the computational requirements for $N > 2$) and focused on three key values of Stark strength: $U = 0, -0.9$ and 0.9 . Here, $U = 0.9$ corresponds to the maximum output work, whereas $U = -0.9$ corresponds to the highest efficiency. To explore the performance limits of the thermal engine under finite-time operation, we employed the optimized coupling strength, $\lambda = 0.47$ for $U = 0$, $\lambda = 0.21$

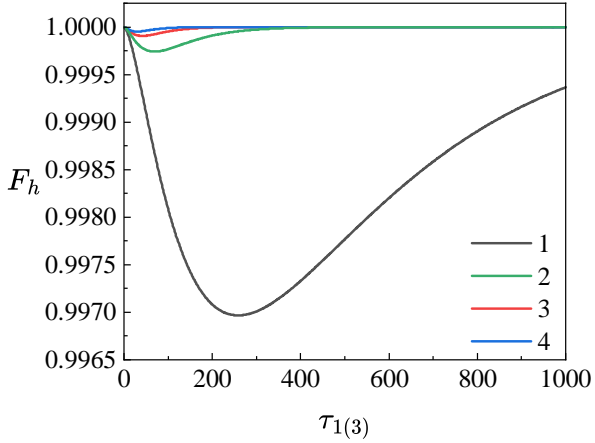


FIG. 7. Fidelity for Fidelity between $\rho_{\tau_0}^{m-1}$ and $\rho_{\tau_0}^m$ as a function of the stroke time $\tau_{1(3)}$, where the number of iterative cycles $m = 1, 2, 3, 4$ corresponds to the solid lines in black, red, blue, and green, respectively. The additional system parameters are $N = 2$, $\lambda = 0.47$, $\omega_h = 2\omega$, $U = 0$, $\omega_c = \omega$, $\omega = 1$, $T_c = 0.1$, and $T_h = 0.5$.

for $U = 0.9$, and $\lambda = 0.68$ for $U = -0.9$, which maximizes the output work and efficiency under quasistatic conditions. Under finite-time conditions, incomplete thermalization during the isochoric process and nonadiabatic excitation transitions during adiabatic strokes lead to entropy generation and quantum friction. To quantify these irreversible effects, entropy production (Eq. (16)) and quantum friction (Eq. (18)) are used as performance metrics for the heat engine. As shown in Fig. 8(c), (d), (g), (h), (k), and (l), both quantum friction and entropy production monotonically decrease with increasing stroke duration $\tau_{2(4)}$ and gradually stabilize after their minimum values are reached. Figures. 8(a), (b), (e), (f), (i), and (j) indicate that the output work of the system increases monotonically with increasing stroke duration $\tau_{2(4)}$ and gradually reaches saturation. These results demonstrate that by optimizing the Stark strength U and interaction strength λ , when the isochoric process time $\tau_{1(3)}$ is between 1000 and 4000 and the adiabatic process time $\tau_{2(4)} < 20$, the heat engine achieves stable performance after five working cycles are completed. Comparing each column of the plots for $U = 0, 0.9$ and -0.9 in Fig. 8 reveals that as U increases, the heat engine requires a longer adiabatic process time $\tau_{2(4)}$ to achieve a stable operating state and effectively reduces quantum friction.

In particular, Figs. 8(a), (e), and (i) show that when the isochoric process time $\tau_{1(3)}$ is set to 1000, 2000, 3000, or 4000, the corresponding output work W of the heat engine increases. Under finite-time conditions, power is a key parameter characterizing the performance of Otto heat engines and is influenced by the adiabatic stroke time $\tau_{2(4)}$, isochoric stroke time $\tau_{1(3)}$, Stark field strength and coupling strength λ , as illustrated in Fig. 9. As $\tau_{2(4)}$ increases, the output power gradu-

ally increases and reaches saturation. Moreover, when $\tau_{1(3)} = 1000, 2000, 3000$ and 4000 , the values at which the power saturates decrease successively, which is contrary to the results of the output work shown in Fig. 8. When $(U = 0$ and $U = 0.9$, the power of the heat engine is significantly greater than that when $U = -0.9$. The maximum power output occurs at $U = 0$ and $\lambda = 0.58$ [see the black solid line in Fig. 9(a)]. For $U = 0.9$ and $\lambda = 0.21$, the output power shown in Fig. 9(b) is nearly identical to that shown in Fig. 9(a). Crucially, modulating the Stark intensity achieves similar output power, while the coupling strength λ is significantly reduced, which is beneficial to the design of heat engines.

There exists a time-asymmetric stroke heat engine model [67, 77] characterized by independent adjustment of the durations of the two adiabatic strokes. Using the duration of the second adiabatic stroke τ_4 as the horizontal axis and the duration of the fourth adiabatic stroke τ_2 as the vertical axis, the output work and efficiency exhibit obvious asymmetry. As shown in Fig. 10(a), the peak output work deviates markedly from the diagonal, exhibiting a stronger dependence on the duration of the second adiabatic stroke τ_2 , and appears in the region where τ_2 is relatively small. The efficiency peak also displays asymmetry and depends more on the duration of the fourth adiabatic stroke τ_4 , as shown in Fig. 10(b). Consequently, targeted adjustment of the time allocation between these adiabatic strokes maximizes both the power output and the thermodynamic efficiency.

VI. CONCLUSION

Numerical simulations of a quantum Otto engine were performed using the DS model as the working substance. The effects of the Stark field strength, coupling strength, adiabatic stroke duration, isochoric stroke duration, and number of atoms in the DS model on the heat engine's output work, efficiency, and power output were investigated. Within the infinite-time thermodynamics framework, regulating the Stark field strength and coupling strength enables conversion between four distinct operating modes and allows optimization of the heat engine's operating state to maximize output work and efficiency. The calculation results show that the maximum values of output work and efficiency occur near the coupling strength λ_c corresponding to the superradiant phase transition. Within the range of $[-0.9, 0.9]$, a larger U can increase the heat engine's output work, whereas a smaller U is beneficial for enhancing its efficiency. Applying different Stark field strengths U_2 and U_4 to control the adiabatic expansion and compression processes facilitates optimization of the heat engine performance. Additionally, in the DS model, an increase in the number of atoms also helps to increase the output work and efficiency of the heat engine. A complete cycle of an actual heat engine takes a finite amount of time. Within the infinite-time thermodynamics framework, the

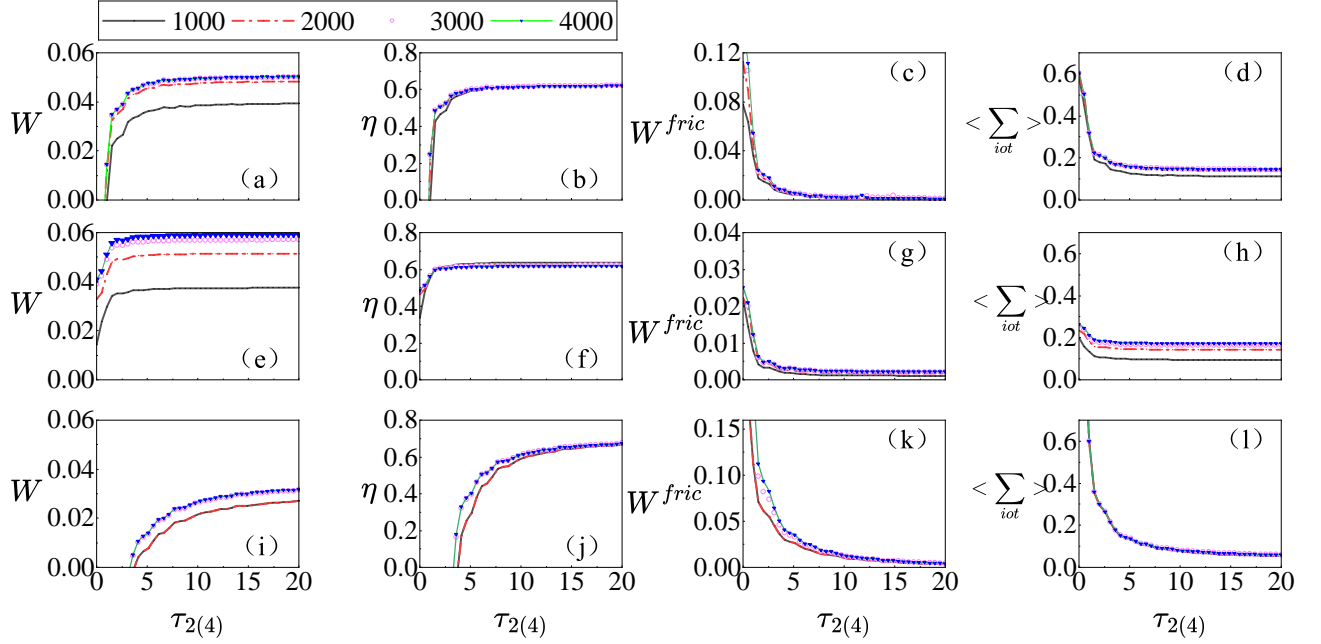


FIG. 8. Parameters that characterize the performance of the heat engine: work output (first column), engine efficiency (second column), quantum friction (third column), and entropy production (fourth column) as functions of the adiabatic driving time $\tau_2 = \tau_4$, whereas curves with different colors correspond to different durations of the isochoric thermalization time $\tau_1 = \tau_3$. Parameters used in the calculations: first row (a)-(d) $\lambda = 0.47$, $U = 0$; second row combination (e)-(h) $\lambda = 0.21$, $U = 0.9$; and third row (i)-(l) $\lambda = 0.68$, $U = -0.9$. Other parameters include $\omega_h = 2\omega$, $\omega_c = \omega$, $\omega = 1$, $T_c = 0.1$, and $T_h = 0.5$.

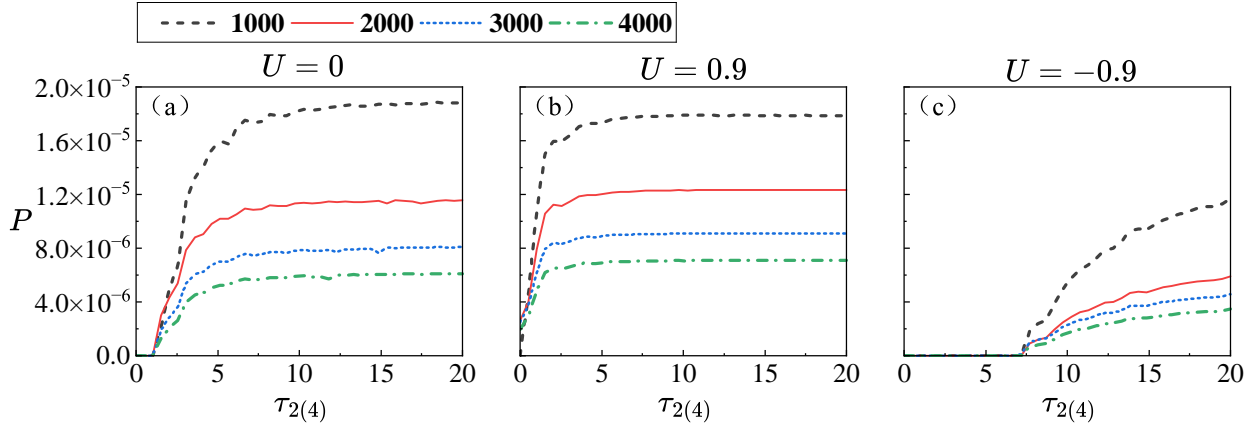


FIG. 9. Power curves as a function of the adiabatic stroke time $\tau_{2(4)}$, with the isochoric stroke times $\tau_{1(3)} = 1000, 2000, 3000$ and 4000 corresponding to the black shot, red, blue and green lines, respectively. The Stark strength U and coupling strength λ in (a), (b) and (c) are $\lambda = 0.58$ for $U = 0$, $\lambda = 0.21$ for $U = 0.9$ and $\lambda = 0.68$ for $U = -0.9$, respectively. Other parameters include $\omega_h = 2\omega$, $\omega_c = \omega$, $\omega = 1$, $T_c = 0.1$, and $T_h = 0.5$.

output work and efficiency of the heat engine are less than those under infinite-time conditions, which is due to entropy generation and quantum friction arising during the nonequilibrium evolution of the system's quantum state. By adjusting the isochoric stroke time $\tau_{1(3)}$, adiabatic stroke time $\tau_{2(4)}$, Stark field strength and coupling strength, the heat engine can achieve stable output

work, efficiency, and power after 5 complete cycles. The increases in $\tau_{1(3)}$ and $\tau_{2(4)}$ cause the output work and efficiency to reach saturation. A reduction in $\tau_{1(3)}$ is beneficial for increasing power. A larger U makes it possible to design a heat engine with relatively high efficiency under conditions of low coupling strength. Moreover, a time-asymmetric heat engine with independent regulation of

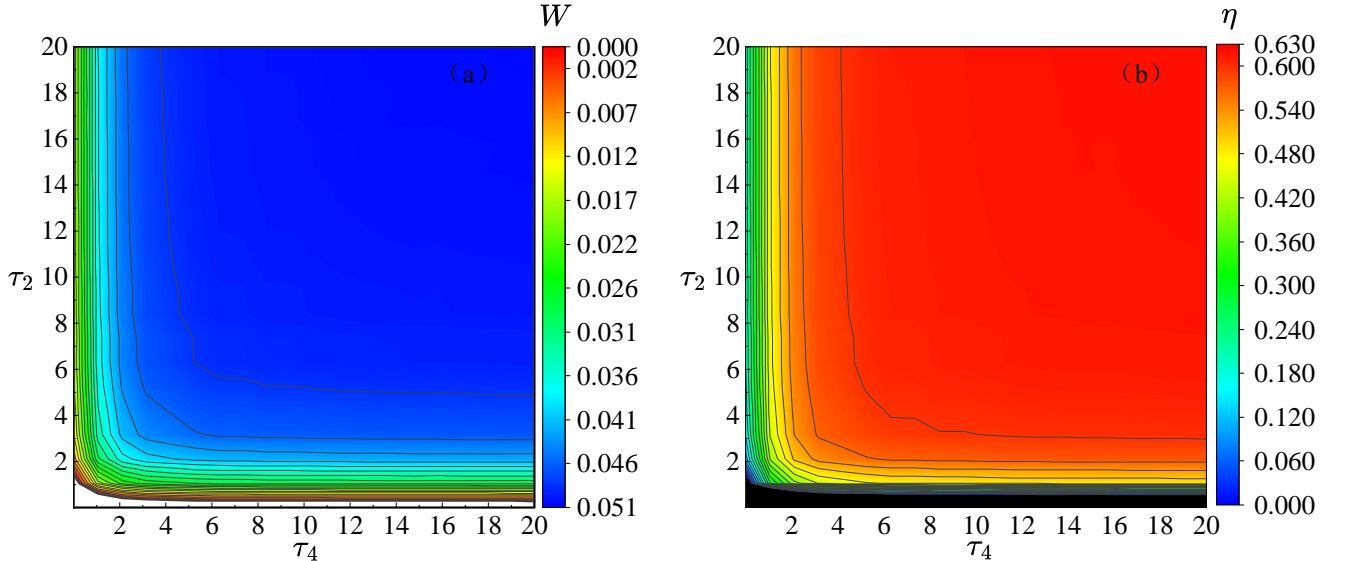


FIG. 10. (a) and (b) Two-dimensional heatmap distributions of the output work (a) and efficiency (b) of the asymmetric DS quantum Otto heat engine in the $\tau_2 - \tau_4$ stroke time space. The horizontal axis represents the duration of the fourth stroke τ_4 , whereas the vertical axis represents the duration of the second stroke τ_2 ; the color scale quantifies the performance. The additional system parameters are $\lambda = 0.48$, $U = 0$, $\omega_h = 2\omega$, $\omega_c = \omega$, $\omega = 1$, $T_c = 0.1$, and $T_h = 0.5$.

the adiabatic compression time τ_2 and adiabatic expansion time τ_4 is favorable for optimizing the output work and efficiency of the heat engine. The work presented in this paper contributes to the design of high-performance quantum heat engines.

ACKNOWLEDGMENTS

We acknowledge the useful discussions with Jiasen Jin and He-Guang Xu. This work is supported by the Science and Technology Projects of the China Southern Power Grid (YNKJXM20220050).

[1] JE Geusic, EO Schulz-DuBios, and HED Scovil. Quantum equivalent of the carnot cycle. *Physical Review*, 156(2):343, 1967.

[2] Ronnie Kosloff. Quantum thermodynamics: A dynamical viewpoint. *Entropy*, 15(6):2100–2128, 2013.

[3] AV Dodonov, D Valente, and T Werlang. Quantum power boost in a nonstationary cavity-qed quantum heat engine. *Journal of Physics A: Mathematical and Theoretical*, 51(36):365302, 2018.

[4] Timo Kerremans, Peter Samuelsson, and Patrick Potts. Probabilistically violating the first law of thermodynamics in a quantum heat engine. *SciPost Physics*, 12(5):168, 2022.

[5] Hao Wang, Sanqiu Liu, and Jizhou He. Thermal entanglement in two-atom cavity qed and the entangled quantum otto engine. *Physical Review E—Statistical, Nonlinear, and Soft Matter Physics*, 79(4):041113, 2009.

[6] Lorenzo Buffoni, Andrea Solfanelli, Paola Verrucchi, Alessandro Cuccoli, and Michele Campisi. Quantum measurement cooling. *Physical review letters*, 122(7):070603, 2019.

[7] Johannes Roßnagel, Obinna Abah, Ferdinand Schmidt-Kaler, Kilian Singer, and Eric Lutz. Nanoscale heat engine beyond the carnot limit. *Physical review letters*, 112(3):030602, 2014.

[8] Jan Klaers, Stefan Faelt, Atac Imamoglu, and Emre Togan. Squeezed thermal reservoirs as a resource for a nanomechanical engine beyond the carnot limit. *Physical Review X*, 7(3):031044, 2017.

[9] Gleb Maslennikov, Shiqian Ding, Roland Hablützel, Jaren Gan, Alexandre Roulet, Stefan Nimmrichter, Jibo Dai, Valerio Scarani, and Dzmitry Matsukevich. Quantum absorption refrigerator with trapped ions. *Nature communications*, 10(1):202, 2019.

[10] Keye Zhang, Francesco Bariani, and Pierre Meystre. Quantum optomechanical heat engine. *Physical review letters*, 112(15):150602, 2014.

[11] Keye Zhang, Francesco Bariani, and Pierre Meystre. Theory of an optomechanical quantum heat engine. *Physical Review A*, 90(2):023819, 2014.

[12] Jean-Philippe Brantut, Charles Grenier, Jakob Meineke, David Stadler, Sebastian Krinner, Corinna Kollath, Tilman Esslinger, and Antoine Georges. A thermoelectric heat engine with ultracold atoms. *Science*, 342(6159):713–715, 2013.

[13] Jonne V Koski, Aki Kutvonen, Ivan M Khaymovich, Tapio Ala-Nissila, and Jukka P Pekola. On-chip maxwell’s demon as an information-powered refrigerator. *Physical review letters*, 115(26):260602, 2015.

[14] JP Pekola, DS Golubev, and DV Averin. Maxwell's demon based on a single qubit. *Physical Review B*, 93(2):024501, 2016.

[15] Ronnie Kosloff and Yair Rezek. The quantum harmonic otto cycle. *Entropy*, 19(4):136, 2017.

[16] Sebastian Deffner and Steve Campbell. *Quantum Thermodynamics: An introduction to the thermodynamics of quantum information*. Morgan & Claypool Publishers, 2019.

[17] George Thomas, Manik Banik, and Sibasish Ghosh. Implications of coupling in quantum thermodynamic machines. *Entropy*, 19(9):442, 2017.

[18] S Hamedani Raja, Sabrina Maniscalco, Gheorghe-Sorin Paraoanu, Jukka P Pekola, and N Lo Gullo. Finite-time quantum stirling heat engine. *New Journal of Physics*, 23(3):033034, 2021.

[19] George Thomas and Ramandeep S Johal. Friction due to inhomogeneous driving of coupled spins in a quantum heat engine. *The European Physical Journal B*, 87:1–6, 2014.

[20] Antonio Alegre, Fernando Galve, N Lo Gullo, Luca Dell'Anna, Francesco Plastina, and Roberta Zambrini. Quantum otto cycle with inner friction: finite-time and disorder effects. *New Journal of Physics*, 17(7):075007, 2015.

[21] Francesco Plastina, Antonio Alegre, Tony JG Apollaro, Giovanni Falcone, Gianluca Francica, Fernando Galve, Nicolino Lo Gullo, and Roberta Zambrini. Irreversible work and inner friction in quantum thermodynamic processes. *Physical review letters*, 113(26):260601, 2014.

[22] Obinna Abah and Mauro Paternostro. Shortcut-to-adiabaticity otto engine: A twist to finite-time thermodynamics. *Physical Review E*, 99(2):022110, 2019.

[23] Naoto Shiraishi, Keiji Saito, and Hal Tasaki. Universal trade-off relation between power and efficiency for heat engines. *Physical review letters*, 117(19):190601, 2016.

[24] Tim Keller, Thomás Fogarty, Jing Li, and Thomas Busch. Feshbach engine in the thomas-fermi regime. *Physical Review Research*, 2(3):033335, 2020.

[25] Maron F Anka, Thiago R de Oliveira, and Daniel Jonathan. Measurement-based quantum heat engine in a multilevel system. *Physical Review E*, 104(5):054128, 2021.

[26] Nathan M Myers, Obinna Abah, and Sebastian Deffner. Quantum otto engines at relativistic energies. *New journal of physics*, 23(10):105001, 2021.

[27] Barış Çakmak and Özgür E Müstecaplıoğlu. Spin quantum heat engines with shortcuts to adiabaticity. *Physical Review E*, 99(3):032108, 2019.

[28] John PS Peterson, Tiago B Batalhão, Marcela Herrera, Alexandre M Souza, Roberto S Sarthour, Ivan S Oliveira, and Roberto M Serra. Experimental characterization of a spin quantum heat engine. *Physical review letters*, 123(24):240601, 2019.

[29] Thomás Fogarty and Thomas Busch. A many-body heat engine at criticality. *Quantum Science and Technology*, 6(1):015003, 2020.

[30] Robert H Dicke. Coherence in spontaneous radiation processes. *Physical review*, 93(1):99, 1954.

[31] FT Hioe. Phase transitions in some generalized dicke models of superradiance. *Physical Review A*, 8(3):1440, 1973.

[32] Yo K Wang and FT Hioe. Phase transition in the dicke model of superradiance. *Physical Review A*, 7(3):831, 1973.

[33] Dasom Kim, Sohail Dasgupta, Xiaoxuan Ma, Joong-Mok Park, Hao-Tian Wei, Xinwei Li, Liang Luo, Jacques Doumani, Wanting Yang, Di Cheng, et al. Observation of the magnonic dicke superradiant phase transition. *Science advances*, 11(14):eabd1691, 2025.

[34] Anil Kumar Chauhan, A Kani, and Jason Twamley. Enhancing macroscopic multimode entanglement through many-body interactions in cavity magnomechanics. *Physical Review A*, 111(3):033505, 2025.

[35] David Guéry-Odelin, Andreas Ruschhaupt, Anthony Kiely, Erik Torrontegui, Sofia Martínez-Garaot, and Juan Gonzalo Muga. Shortcuts to adiabaticity: Concepts, methods, and applications. *Reviews of Modern Physics*, 91(4):045001, 2019.

[36] Adolfo del Campo, Aurélia Chenu, Shujin Deng, and Haibin Wu. Friction-free quantum machines. *Thermodynamics in the quantum regime: fundamental aspects and new directions*, pages 127–148, 2018.

[37] Erik Torrontegui, Sara Ibáñez, Sofia Martínez-Garaot, Michele Modugno, Adolfo del Campo, David Guéry-Odelin, Andreas Ruschhaupt, Xi Chen, and Juan Gonzalo Muga. Shortcuts to adiabaticity. In *Advances in atomic, molecular, and optical physics*, volume 62, pages 117–169. Elsevier, 2013.

[38] Paolo Abiuso and Martí Perarnau-Llobet. Optimal cycles for low-dissipation heat engines. *Physical review letters*, 124(11):110606, 2020.

[39] A del Campo, John Goold, and Mauro Paternostro. More bang for your buck: Super-adiabatic quantum engines. *Scientific reports*, 4(1):6208, 2014.

[40] Adolfo Del Campo. Shortcuts to adiabaticity by counter-adiabatic driving. *Physical review letters*, 111(10):100502, 2013.

[41] Giulia Piccitto, Michele Campisi, and Davide Rossini. The ising critical quantum otto engine. *New Journal of Physics*, 24(10):103023, 2022.

[42] Yu-Han Ma, Shan-He Su, and Chang-Pu Sun. Quantum thermodynamic cycle with quantum phase transition. *Physical Review E*, 96(2):022143, 2017.

[43] Yang-Yang Chen, Gentaro Watanabe, Yi-Cong Yu, Xi-Wen Guan, and Adolfo del Campo. An interaction-driven many-particle quantum heat engine and its universal behavior. *npj Quantum Information*, 5(1):88, 2019.

[44] Revathy B. S, Victor Mukherjee, Uma Divakaran, and Adolfo del Campo. Universal finite-time thermodynamics of many-body quantum machines from kibble-zurek scaling. *Physical Review Research*, 2(4):043247, 2020.

[45] BS Revathy, Harsh Sharma, and Uma Divakaran. Improving performance of quantum heat engines using modified otto cycle. *Journal of Physics A: Mathematical and Theoretical*, 57(16):165302, 2024.

[46] Qing-Hu Chen, Lei Li, Tao Liu, and Ke-Lin Wang. The spectrum in qubit-oscillator systems in the ultrastrong coupling regime. *Chinese Physics Letters*, 29(1):014208, 2012.

[47] JM Fink, M Göppl, M Baur, R Bianchetti, Peter J Leek, Alexandre Blais, and Andreas Wallraff. Climbing the jaynes-cummings ladder and observing its nonlinearity in a cavity qed system. *Nature*, 454(7202):315–318, 2008.

[48] Qing-Hu Chen, Yu-Yu Zhang, Tao Liu, and Ke-Lin Wang. Numerically exact solution to the finite-size dicke

model. *Physical Review A—Atomic, Molecular, and Optical Physics*, 78(5):051801, 2008.

[49] Clive Emery and Tobias Brandes. Quantum chaos triggered by precursors of a quantum phase transition: the dicke model. *Physical review letters*, 90(4):044101, 2003.

[50] Alexandre Le Boité, Myung-Joong Hwang, Hyunchul Nha, and Martin B Plenio. Fate of photon blockade in the deep strong-coupling regime. *Physical Review A*, 94(3):033827, 2016.

[51] Tian Ye, Chen Wang, and Qing-Hu Chen. Quantum phase transition of light in the dissipative rabi-hubbard lattice: A dressed-master-equation perspective. *Physical Review A*, 104(5):053708, 2021.

[52] Alessio Settineri, Vincenzo Macrì, Alessandro Ridolfo, Omar Di Stefano, Anton Frisk Kockum, Franco Nori, and Salvatore Savasta. Dissipation and thermal noise in hybrid quantum systems in the ultrastrong-coupling regime. *Physical Review A*, 98(5):053834, 2018.

[53] Barry M Garraway. The dicke model in quantum optics: Dicke model revisited. *Philosophical Transactions of the Royal Society A: Mathematical, Physical and Engineering Sciences*, 369(1939):1137–1155, 2011.

[54] Sarang Gopalakrishnan, Benjamin L Lev, and Paul M Goldbart. Frustration and glassiness in spin models with cavity-mediated interactions. *Physical review letters*, 107(27):277201, 2011.

[55] VM Bastidas, C Emery, B Regler, and T Brandes. Nonequilibrium quantum phase transitions in the dicke model. *Physical review letters*, 108(4):043003, 2012.

[56] AS Abdel-Rady, Samia SA Hassan, Abdel-Nasser A Osman, and Ahmed Salah. Quantum phase transition and berry phase of the dicke model in the presence of the stark-shift. *International Journal of Modern Physics B*, 31(12):1750091, 2017.

[57] Fengchun Mu, Ya Gao, Hongda Yin, and Gangcheng Wang. Dicke state generation via selective interactions in a dicke-stark model. *Optics Express*, 28(26):39574–39585, 2020.

[58] Weilin Wang, Ronghai Liu, Fangcheng Qiu, Mingshu Zhao, Jinying Ma, and Zhanyuan Yan. Superradiant phase transition and statistical properties in dicke-stark model. *arXiv preprint arXiv:2508.08860*, 2025.

[59] Gavin McCauley, Benjamin Cruikshank, Denys I Bondar, and Kurt Jacobs. Accurate lindblad-form master equation for weakly damped quantum systems across all regimes. *npj Quantum Information*, 6(1):74, 2020.

[60] He-Guang Xu, Jiasen Jin, GDM Neto, and Norton G de Almeida. Universal quantum otto heat machine based on the dicke model. *Physical Review E*, 109(1):014122, 2024.

[61] He-Guang Xu, Jiasen Jin, Norton G de Almeida, and GD de Moraes Neto. Exploring the role of criticality in the quantum otto cycle fueled by the anisotropic quantum rabi-stark model. *Physical Review B*, 110(13):134318, 2024.

[62] Vittorio Gorini, Andrzej Kossakowski, and Ennackal Chandy George Sudarshan. Completely positive dynamical semigroups of n-level systems. *Journal of Mathematical Physics*, 17(5):821–825, 1976.

[63] Goran Lindblad. On the generators of quantum dynamical semigroups. *Communications in mathematical physics*, 48:119–130, 1976.

[64] Ulrich Weiss. *Quantum dissipative systems*. World Scientific, 2012.

[65] Heinz-Peter Breuer and Francesco Petruccione. *The theory of open quantum systems*. OUP Oxford, 2002.

[66] Tien D Kieu. The second law, maxwell’s demon, and work derivable from quantum heat engines. *Physical review letters*, 93(14):140403, 2004.

[67] Rahul Shastri and B Prasanna Venkatesh. Optimization of asymmetric quantum otto engine cycles. *Physical Review E*, 106(2):024123, 2022.

[68] Vasco Cavina, Andrea Mari, and Vittorio Giovannetti. Slow dynamics and thermodynamics of open quantum systems. *Physical review letters*, 119(5):050601, 2017.

[69] Yu-Han Ma, Dazhi Xu, Hui Dong, and Chang-Pu Sun. Universal constraint for efficiency and power of a low-dissipation heat engine. *Physical Review E*, 98(4):042112, 2018.

[70] Yu-Han Ma, Dazhi Xu, Hui Dong, and Chang-Pu Sun. Optimal operating protocol to achieve efficiency at maximum power of heat engines. *Physical Review E*, 98(2):022133, 2018.

[71] Roie Dann, Ander Tobalina, and Ronnie Kosloff. Fast route to equilibration. *Physical Review A*, 101(5):052102, 2020.

[72] G Alvarado Barrios, F Albarrán-Arriagada, FJ Peña, E Solano, and JC Retamal. Light-matter quantum otto engine in finite time. *arXiv preprint arXiv:2102.10559*, 2021.

[73] Hisaharu Umegaki. Conditional expectation in an operator algebra. *Tohoku Mathematical Journal, Second Series*, 6(2-3):177–181, 1954.

[74] Vlatko Vedral. The role of relative entropy in quantum information theory. *Reviews of Modern Physics*, 74(1):197, 2002.

[75] Masahito Hayashi. *Quantum information theory*. Springer, 2017.

[76] Yang Xiao, Dehua Liu, Jizhou He, Lin Zhuang, Wu-Ming Liu, L-L Yan, and Jianhui Wang. Thermodynamics and fluctuations in finite-time quantum heat engines under reservoir squeezing. *Physical Review Research*, 5(4):043185, 2023.

[77] Yuanjian Zheng, Peter Hänggi, and Dario Poletti. Occurrence of discontinuities in the performance of finite-time quantum otto cycles. *Physical Review E*, 94(1):012137, 2016.